

LoGoColor: Local-Global 3D Colorization for 360° Scenes

Yeonjin Chang Juhwan Cho Seunghyeon Seo Wonsik Shin Nojun Kwak

Seoul National University

{yjean8315|hj99cho|zzzlssh|wonsikshin|nojunk}@snu.ac.kr

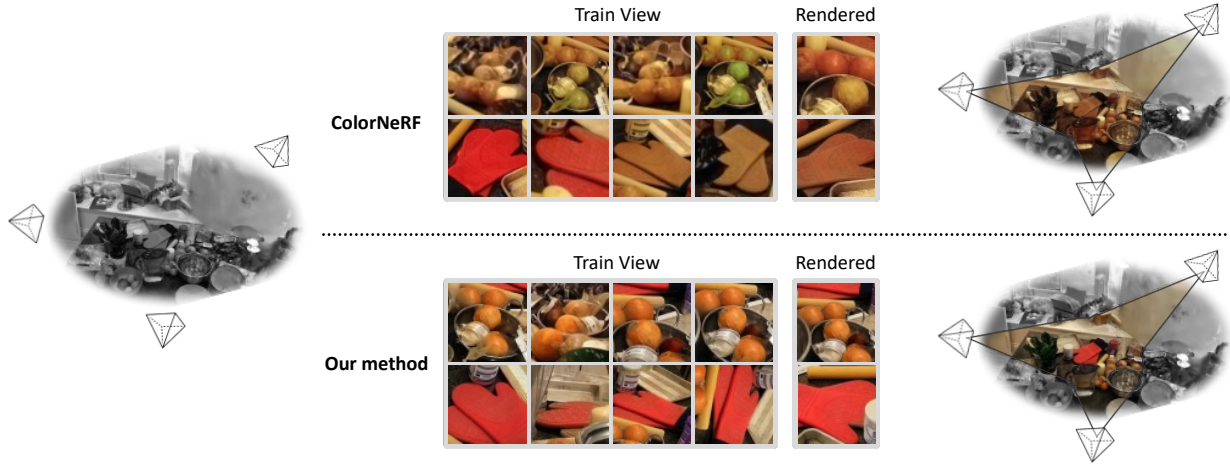


Figure 1. **Teaser** – We propose *LoGoColor* to achieve color-rich 3D colorization by minimizing guidance from image models. This avoids the guidance-averaging of prior works, which relied on inconsistent image model outputs and led to monotonous results. To do so, we explicitly handle consistency with a Local-Global approach, ensuring both intra- and inter- subscene consistency.

Abstract

Single-channel 3D reconstruction is widely used in fields such as robotics and medical imaging. While this line of work excels at reconstructing 3D geometry, the outputs are not colored 3D models, thus 3D colorization is required for visualization. Recent 3D colorization studies address this problem by distilling 2D image colorization models. However, these approaches suffer from an inherent inconsistency of 2D image models. This results in colors being averaged during training, leading to monotonous and oversimplified results, particularly in complex 360° scenes. In contrast, we aim to preserve color diversity by generating a new set of consistently colorized training views, thereby bypassing the averaging process. Nevertheless, eliminating the averaging process introduces a new challenge: ensuring strict multi-view consistency across these colorized views. To achieve this, we propose *LoGoColor*, a pipeline designed to preserve color diversity by eliminating this guidance-averaging process with a ‘Local-Global’ approach: we partition the scene into subscenes and explicitly tackle both

inter-subscene and intra-subscene consistency using a fine-tuned multi-view diffusion model. We demonstrate that our method achieves quantitatively and qualitatively more consistent and plausible 3D colorization on complex 360° scenes than existing methods, and validate its superior color diversity using a novel Color Diversity Index.

1. Introduction

Recent advancements in 3D reconstruction, driven by Neural Radiance Fields (NeRF) [37] and 3D Gaussian Splatting (3DGS) [23], have enabled high-fidelity novel view synthesis. These breakthroughs have spurred a wide range of subsequent research, including dynamic scene representation [13, 31], efficient training [12, 19], scene editing [54, 64], and 3d scene generation [42, 66], increasing their applicability in VR/AR.

One line of subsequent research has focused on multi-view reconstruction from single-channel images, with prior works focusing on optimizing 3D models from thermal or (near-)infrared images, or reconstructing 3D volumes from

X-ray images in the medical domain [6, 28, 34, 60]. However, they primarily focus on generating 3D geometry for specific applications, such as robot manipulation [49] or medical assistance [5]. While effective for these specific tasks, the resulting single-channel models lack the rich visual data of full-color RGB models. This limits their versatility for general-purpose applications like VR/AR and their compatibility with standard 3D pipelines. To bridge this gap and make these single-channel 3D reconstructions truly versatile, a robust 3D colorization step is essential.

3D colorization task, however, presents a crucial challenge beyond the vividness and plausibility required in 2D image colorization: ensuring **color consistency across views**. Existing 3D colorization methods achieve this by leveraging image model outputs, either by iteratively updating the 3D representation with local patch outputs [10], or by training from pre-generated ones [11]. However, these approaches essentially average the outputs of an image colorization model, either across iterations or training views. This reliance on averaging, while effective at achieving consistency, implicitly assumes a restricted color distribution. This assumption breaks down in 360-degree real-world scenes, which are often composed of numerous distinct objects and complex geometric regions. Consequently, this approach fails to robustly colorize these intricate areas, resulting in muted and oversimplified results as shown in Fig. 1.

In this work, we rethink 3D consistency to robustly colorize complex 360-degree scenes. To preserve their natural color diversity, we minimize independent guidance from image colorization models and eliminate the guidance-averaging process. Instead, we design our pipeline to generate a new set of consistently colorized training views, with minimal reliance on the image model knowledge. While this approach bypasses the averaging issue, it shifts the challenge to how we generate these training views to be *consistent*. To address this, we propose *LoGoColor*, a Local-Global approach designed to achieve consistency without resorting to averaging. We partition the scene into subscenes and explicitly tackle both inter-subscene (global) and intra-subscene (local) consistency, using a fine-tuned multi-view diffusion model to learn and ensure these relationships.

Specifically, our pipeline begins by reconstructing a geometry-only 3D model from the single-channel inputs. Leveraging the training view cameras and the learned geometry, we then apply our *View-based Subscene Decomposition* method to partition the scene into subscenes that maximize coverage while minimizing overlap. For each subscene, we select a representative base view and colorize it with an image colorization model. We then calibrate these base views with a multi-view diffusion model that enforces global consistency among subscenes. The calibrated base views serve as color references for the subsequent colorization of all training views, yielding globally and locally con-

sistent colorized images.

We demonstrate with experiments that our method yields 3D models with diverse and consistent color from single-channel images. By comparing with existing work [10, 11], we show both qualitatively and quantitatively that our model achieves superior color diversity. To quantify this improvement, we propose the *Color Diversity Index (CDI)*, a novel metric specifically designed to evaluate the richness of the color distribution. Notably, even when we adapt these baselines to the 3DGS framework to enhance their geometric reconstruction, their inherent averaging process inevitably leads to monotonous colorization. In contrast, our method successfully preserves the rich color diversity of the scene. We also demonstrate the effectiveness of our Local-Global approach through ablation studies. Finally, we reconstruct colorized 3D models from thermal multi-view images demonstrating that our method applies robustly to single-channel image modalities.

2. Related Work

2.1. 3D reconstruction

Reconstructing 3D scenes from 2D observations is a longstanding problem in computer vision, and recent years have seen significant progress through neural representations. Neural Radiance Fields (NeRF) [37] have emerged as a dominant framework by learning volumetric radiance fields rendered via differentiable volume rendering. Since its introduction, NeRF has been extended in various directions: few-shot reconstruction [46, 47, 58, 62], scene generalization [8, 43, 62], dynamic and unbounded scenes [2, 13], and faster optimization [38, 61]. More recently, 3D Gaussian Splatting (3DGS) [23] has gained attention as a real-time alternative to NeRF, representing scenes with rasterized Gaussian primitives instead of volumetric fields. Its efficiency has sparked numerous follow-ups on anti-aliasing [29, 57, 63], 3D content generation [30, 50, 65, 69], dynamic scenes [53, 56, 59], and so on. In our work, we shift focus to single-channel 3D reconstructions, where geometry is recovered without color. Unlike the above methods that jointly learn color and shape, our method addresses the open challenge of colorizing geometry-only 3D scenes in a globally and locally consistent manner.

2.2. Single channel 3D reconstruction

The Single-channel 3D reconstruction comes from the limits of RGB and depth sensors. While RGB and depth modalities often degrade in such environments, thermal and infrared (IR) signals remain robust, enabling geometry inference directly from intensity variation. Early studies combined thermal or IR cues with photogrammetry to jointly recover geometry and temperature [4, 21], or employed thermal-only silhouette intersection for volumetric recov-

ery [9]. Similar attempts using near-infrared (NIR) polarization [28] further demonstrate that single-channel cues can convey geometric information.

Recently, radiance based representations such as NeRF and 3DGS have extended these ideas. Thermal-NeRF and ThermalGS [34, 60] reconstruct the geometry of the scene and thermal emission directly from the infrared input. However, these neural single-channel approaches still lack realistic color and cues, leading to less fidelity than multi-modal reconstructions. Our work addresses this limitation by coupling single-channel 3D representations with *colorization*, producing vivid and plausible color 3D scenes even under low-light, nighttime, or non-visible conditions.

2.3. Image colorization

Colorizing grayscale images into plausible RGB counterparts has been a fundamental challenge in computer vision. Early CNN-based approaches learn the mapping between luminance and chrominance channels [20, 67], and later transformers capture broader spatial dependencies [26]. Adversarial methods further enhance realism by training generative models to produce sharper and more vivid colors [39, 68]. Diffusion models [17] have recently reframed colorization as an image-to-image translation task [44], offering greater color fidelity and diversity [41]. However, as all these methods operate in a single-view setting, they inherently fail to ensure cross-view color consistency.

Parallel studies aim to translate single-channel modalities, such as thermal into visible spectra. Early cross-modal mappings [52] learn direct transformations between thermal and RGB domains, while later GAN- and diffusion-based approaches [15, 25] generate visually plausible single-view results but still lacks multi-view color coherence. In contrast, our method colorizes multi-view single-channel inputs—grayscale, thermal, or NIR—to reconstruct consistent and realistic 3D color scenes, providing a unified framework for multi-view colorization in 3D.

2.4. 3D colorization

3D colorization has been extensively studied for point clouds acquired from LiDAR or Time-of-Flight cameras, which inherently lack color information [7, 14, 33, 48]. Recently, there have been attempts to colorize 3D reconstructions derived from grayscale images. Notable works include ColorNeRF [10], which integrates colorization into NeRF by training on image patches processed by an image colorization model, and ChromaDistill [11], which distills chromatic information from pre-generated 2D color views into a Plenoxel representation. However, these methods achieve multi-view consistency primarily by averaging the outputs of 2D image models. In contrast, we propose a Local-Global approach that achieves consistency without averaging, by generating a set of consistently colorized

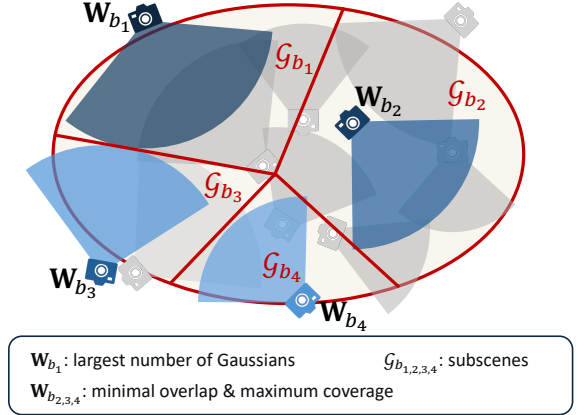


Figure 2. **Our View-based Subscene Decomposition.** – Starting from the base view W_{b1} that observes the largest number of Gaussians, we use a greedy algorithm to iteratively select subsequent base views that maximize coverage while minimizing overlap.

training views, thereby preserving the scene color diversity.

3. Method

We illustrate our proposed approach in Fig. 3. We first optimize single-channel 3D Gaussians from the given single-channel multi-view images (Sec. 3.1). Given the scene geometry and training view cameras, we divide the scene into subscenes that have minimal overlap and whose union covers most of the full scene (Sec. 3.2). For the subsequent Local-Global 3D colorization, we first fine-tune a multi-view diffusion model that colorizes an input image using the color from a reference image (Sec. 3.3). Utilizing this fine-tuned multi-view diffusion model, we perform the Local-Global colorization. We begin by colorizing one base view from each subscene using an image colorization model. To resolve their global inconsistency, we pass them through the fine-tuned multi-view diffusion model to create a globally consistent reference set (Sec. 3.4). Next, to ensure intra-subscene consistency, we again use this fine-tuned model to colorize the remaining training views, referencing the base views (Sec. 3.5). Finally, these consistent views are used as pseudo-ground truth to optimize the color components of the 3D Gaussian model.

3.1. Single-channel 3D Reconstruction

We first aim to reconstruct the scene geometry from given single-channel multi-view images $\mathcal{I}_g = \{I_g^1, I_g^2, \dots, I_g^T\}$, where $I_g^* \in \mathbb{R}^{1 \times H \times W}$. We represent the 3D geometry using a set of single-channel 3D Gaussian primitives, modified from 3D Gaussian Splatting (3DGS) [23]. Standard 3DGS defines each Gaussian primitive with position $\mathbf{x} \in \mathbb{R}^3$, rotation $\mathbf{q} \in \mathbb{R}^4$, scaling $\mathbf{s} \in \mathbb{R}^3$, opacity $\alpha \in \mathbb{R}$, and spherical harmonic coefficients $\mathbf{F}_c \in \mathbb{R}^{3 \times h}$ used to compute its view-dependent color $\mathbf{c} \in \mathbb{R}^3$. Since our input \mathcal{I}_g

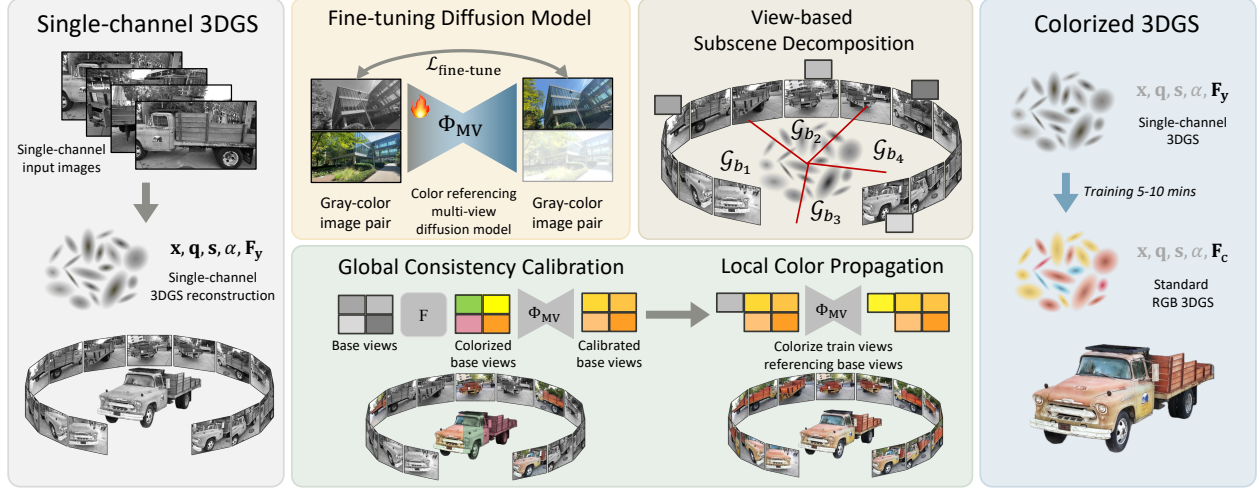


Figure 3. **Overview of LoGoColor**– We first reconstruct single-channel 3D Gaussians from multi-view grayscale images to recover scene geometry. Using this geometry, we decompose the scene into subscenes and select their corresponding base views. In parallel, we fine-tune a multi-view diffusion model to transfer color from reference views. We then calibrate global consistency among the base views and propagate color across all training views, ultimately producing a fully colored 3D Gaussian model.

is single-channel, we adjust this representation by replacing the color component \mathbf{F}_c with a single-channel luminance coefficients $\mathbf{F}_y \in \mathbb{R}^{1 \times h}$, used to compute view-dependent luminance $y \in \mathbb{R}$, while retaining the core geometric parameters $(\mathbf{x}, \mathbf{q}, \mathbf{s}, \alpha)$. We consequently modify the rendering process to compute an α -blended luminance $\hat{\mathbf{Y}}$ for each pixel p :

$$\hat{\mathbf{Y}}(p) = \sum_i^N y_i \alpha'_i \prod_j^{i-1} (1 - \alpha'_j) \quad (1)$$

where N is the number of Gaussian primitives contributing to the pixel p and α' is the projected 2D opacity at pixel p . We optimize all parameters $\mathbf{x}, \mathbf{q}, \mathbf{s}, \alpha, \mathbf{F}_y$ by minimizing a combined \mathcal{L}_1 and D-SSIM loss between the rendered luminance $\hat{\mathbf{Y}}$ and the ground-truth image I_g :

$$\mathcal{L}_{\text{geom}} = (1 - \lambda_s) \mathcal{L}_1(\hat{\mathbf{Y}}, I_g) + \lambda_s \mathcal{L}_{\text{D-SSIM}}(\hat{\mathbf{Y}}, I_g). \quad (2)$$

This process reconstructs a precise geometric foundation for our subsequent ‘‘Local-Global’’ 3D colorization pipeline.

3.2. View-based Subscene Decomposition

We decompose the 360-degree scene into multiple subscenes, based on the 3D Gaussian geometry reconstructed in Sec. 3.1 and the training camera views. We design this decomposition to leverage the prior knowledge of an image colorization model for intricate parts of the complex scene while tackling inter- and intra-subscene consistency. The objective of the decomposition is twofold: 1) ensure maximum coverage across the scene, and 2) find K subscenes that have minimal overlap to prevent potential inconsistencies from multiple reference colors. Directly addressing these conditions on the myriad of Gaussian primitives

is complex, as it involves solving a large-scale partitioning problem on millions of points. Instead, we reframe the problem as partitioning the scene from the perspective of camera poses that represent these Gaussian subsets. Specifically, we associate each camera pose \mathbf{W}_t with its set of visible Gaussian splats (\mathcal{G}_t)—the Gaussians used when rendering the image for that camera. We thus partition the scene by selecting K base views (camera poses) whose corresponding Gaussian sets best satisfy the conditions of maximum coverage and minimal overlap.

We find these base view cameras using a greedy algorithm. First, we select the first base view \mathbf{W}_{b_1} as the camera that observes the largest number of Gaussians. We initialize the covered region as $\mathcal{G}_{\text{covered}} = \mathcal{G}_{b_1}$. Subsequently, for $k = 2$ to K , we iteratively select the next base view \mathbf{W}_{b_k} as the camera $\mathbf{W}_t \in \mathcal{W}$ that maximizes the ratio of newly covered Gaussians to the overlapping Gaussians:

$$\mathbf{W}_{b_k} = \arg \max_{\mathbf{W}_t \in \mathcal{W}} \frac{|\mathcal{G}_t \setminus \mathcal{G}_{\text{covered}}|}{|\mathcal{G}_t \cap \mathcal{G}_{\text{covered}}| + 1} \quad (3)$$

where adding 1 to the denominator prevents division by zero. After selecting \mathbf{W}_{b_k} , we update the set of covered Gaussians: $\mathcal{G}_{\text{covered}} \leftarrow \mathcal{G}_{\text{covered}} \cup \mathcal{G}_{b_k}$. This process yields K base views and their corresponding subscenes that approximate our coverage and overlap goals. See Fig. 2 for a visualization. Note that this greedy selection minimized overlap but does not eliminate it. However, as we describe in Sec. 3.4, any potential inconsistencies arising from this remaining overlap are resolved when we later use these K base views to enforce global (inter-subscene) consistency.

3.3. Multi-view Colorizing Model Fine-tuning

Our Local-Global colorization approach requires a model capable of handling both inter-subscene and intra-subscene consistency while preserving the 3D structure from Sec. 3.1. Diffusion models have proven highly effective for image-to-image translation tasks, including colorization [44], making them a strong candidate for our pipeline. However, unlike standard image-to-image models that process images independently, our approach requires a model that can also ensure color consistency across multiple views of the scene. To achieve this, we adopt the diffusion model SD-Turbo [1, 45] as a base, and fine-tune it following the image-to-image training scheme of pix2pix-Turbo [41]. Crucially, to enable the required multi-view referencing, we integrate a reference mixing layer from DIFIX3D+ [55], which applies self-attention to the reference image I_{ref} to guide the colorization of the single-channel input I_g . We denote this multi-view model as Φ_{MV} .

The fine-tuning process trains Φ_{MV} to generate \hat{I}_c by applying the color of its reference image I_{ref} to the input I_g while preserving structure. To provide explicit guidance for color generation, we compute the loss in the LAB color space, which is more perceptually uniform than the standard RGB color space [67]. We convert both the model output \hat{I}_c and the ground-truth I_c to LAB space. The loss function is then composed of a \mathcal{L}_{L1} loss and an \mathcal{L}_{LPIPS} perceptual loss:

$$\mathcal{L}_{\text{fine-tune}} = \mathcal{L}_{L1}(\hat{I}_c, I_c) + \lambda_{LPIPS} \mathcal{L}_{LPIPS}(\hat{I}_c, I_c) \quad (4)$$

Thanks to the combination of the reference mixing layer architecture and this training objective, Φ_{MV} learns to colorize in a multi-view consistent manner while preserving image structure. This model plays a key role in Sec. 3.4 and Sec. 3.5.

3.4. Global Consistency Calibration

Using the K base views selected in Sec. 3.2, we generate inter-subscene consistent colorized base views, which will be used as references in Sec. 3.5. To achieve this, we first pass the K base views I_g^k through an image colorization model \mathcal{F} to produce initial colorized base views I_c^{tk} :

$$I_c^{tk} = \mathcal{F}(I_g^k) \quad \text{for } k = 1 \dots K \quad (5)$$

However, since the image colorization model \mathcal{F} processes each input I_g^k independently, it does not guarantee inter-subscene consistency among the resulting $\{I_c^{tk}\}$. To resolve this issue, we introduce a global consistency calibration step that iteratively refines each view using our multi-view diffusion model, Φ_{MV} .

Specifically, for each $k \in [1, K]$, we generate a consistent view I_c^k by averaging the initial view I_c^{tk} with a globally-calibrated version. This calibrated version is generated by passing the grayscale k -th view into Φ_{MV} , which

simultaneously references the color from all other $K - 1$ views, $\{I_c^{tj}\}_{j \neq k}$. This entire calibration process for a single view k is defined as:

$$I_c^k = \frac{1}{2} (I_c^{tk} + \Phi_{MV}(\text{Grayscale}(I_c^{tk}), \{I_c^{tj}\}_{j \neq k})) \quad (6)$$

This process is repeated for all K views to create the final consistent set $\{I_c^k\}_{k=1}^K$. Unlike \mathcal{F} , which processes views independently, this mechanism aggregates the color information from all K image model outputs, thereby resolving potential inconsistencies. These resulting inter-subscene consistent base views are then used as references to enforce intra-subscene consistency in Sec. 3.5.

3.5. Local Color Propagation

Using the inter-subscene consistent reference set obtained in Sec. 3.4, we colorize all T training views to ensure intra-subscene consistency. To do this, we use Φ_{MV} to colorize each training view I_g^t . We pass I_g^t as the structure input while providing the entire set of K calibrated base views $\{I_c^k\}$ as the color reference:

$$\hat{I}_c^t = \Phi_{MV}(I_g^t, \{I_c^k\}_{k=1}^K). \quad (7)$$

The resulting image \hat{I}_c^t thus achieves comprehensive consistency: intra-subscene consistency is achieved via the reference-mixing layer to query the relevant colors from the K base views, while inter-subscene consistency is inherited from the globally-calibrated reference set. By repeating this process for all T views, we obtain a set of fully consistent training views, $\hat{\mathcal{I}}_c = \{\hat{I}_c^t\}_{t=1}^T$, for colorizing the single-channel 3D model. Lastly, we use $\hat{\mathcal{I}}_c$ as pseudo-color ground-truth to colorize the single-channel 3D Gaussian model obtained in Sec. 3.1. We freeze the geometry parameters ($\mathbf{x}, \mathbf{q}, \mathbf{S}, \alpha$) and extend the optimized single-channel luminance coefficients $\mathbf{F}_y \in \mathbb{R}^{1 \times h}$ with new, learnable color coefficients $\mathbf{F}_c \in \mathbb{R}^{3 \times h}$. We then optimize only this new color component \mathbf{F}_c . This additional optimization of the colors of Gaussian primitives yields the final colorized 3D model.

4. Experiments

4.1. Experimental setup

Implementation details. We implement our method using the PyTorch framework, based on the official 3DGS implementation. We train the initial single-channel 3DGS model for 30K iterations. For the scene decomposition, we empirically set the number of subscenes $K = 4$ for the Tanks and Temples and Mip-NeRF 360 datasets, and $K = 1$ for the LLFF dataset. For our multi-view colorization model Φ_{MV} , we fine-tune the pre-trained SD-Turbo model [45] by integrating the reference mixing layer from [55]. We train Φ_{MV} for 25K iterations using the AdamW optimizer [35]

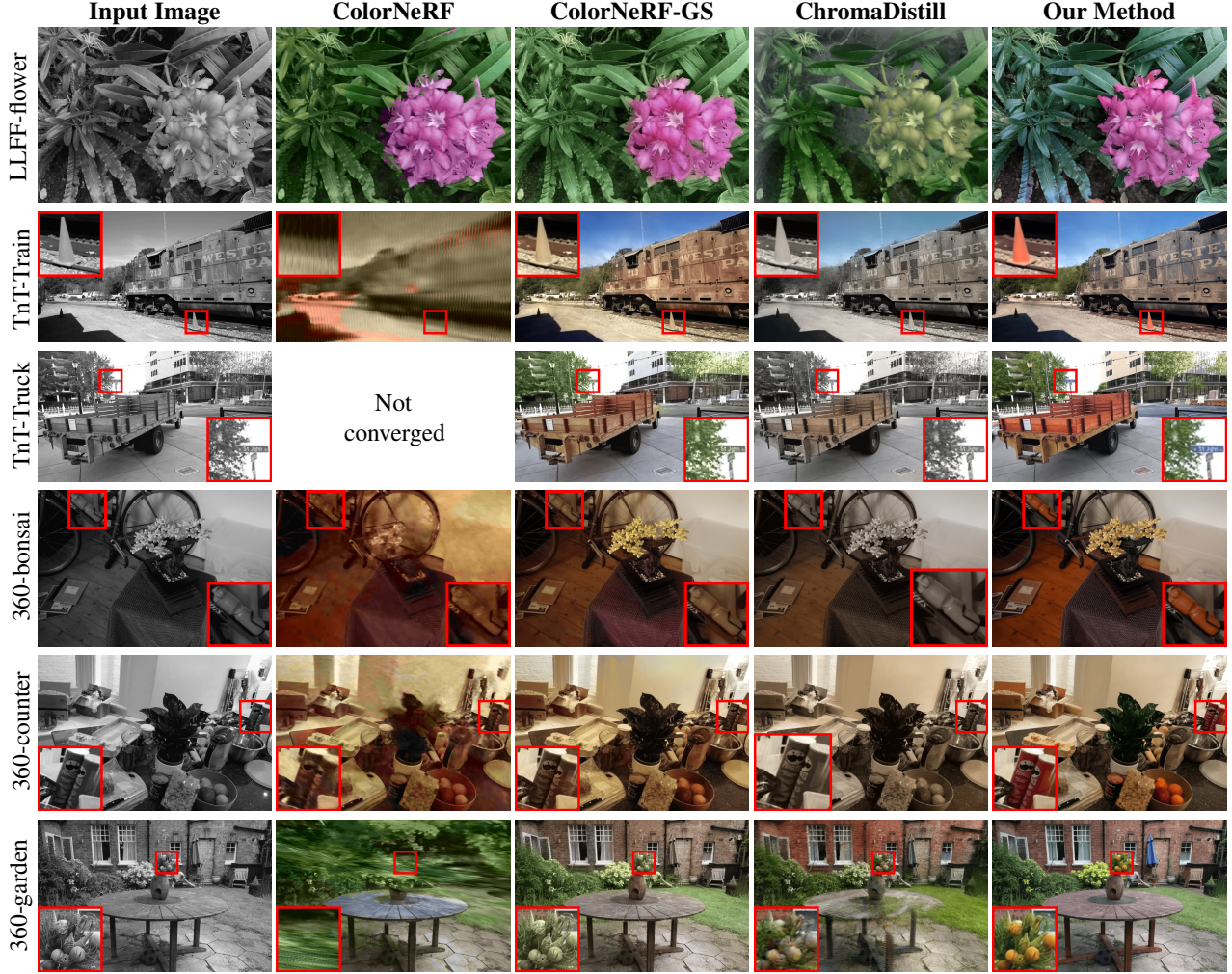


Figure 4. **Qualitative comparison on LLFF, Tanks and Temples (TnT) datasets and Mip-NeRF 360** – While other methods perform reasonably well on the LLFF dataset, they tend to color the leaves in the ‘flower’ scene uniformly. In 360-degree scenes from the TnT and Mip-NeRF 360 datasets, other methods produce monotonous colors. In contrast, our method yields plausible and diverse colors across all regions.

with a constant learning rate 2×10^{-5} . For our fine-tuning loss $\mathcal{L}_{\text{fine-tune}}$, we set the perceptual weight to $\lambda_{\text{LPIPS}} = 1.0$. For our fine-tuning dataset, we utilize two sources, which are mixed during training:

- DL3DV-10K-Benchmark [32]: Used to train multi-view referencing. We select one reference view from each scene and set others as grayscale inputs, yielding 4,920 input pairs.
- Flickr8k [18]: Used to learn the color distribution for image-to-image translation. We apply random crops at 80-100% of the original scale, yielding 8,000 input pairs.

We use DDColor [22] as our plug-and-play image colorization model \mathcal{F} . The final 3D color component optimization is run for 7K iterations. We provide further details in the supplementary material.

Datasets. We evaluate our method on:

- LLFF [36]: forward-facing dataset composed of 24 scenes. We evaluate on 2 scenes – *flower* and *trex* – commonly used in existing works.
- Mip-NeRF 360 [3]: 360-degree dataset composed of 4 indoor and 3 outdoor scenes. We evaluate on the whole dataset.
- Tanks and Temples [24]: 360-degree dataset composed of 20 scenes. We evaluate on 4 scenes – *Horse*, *M60*, *Train* and *Truck* – commonly used in existing works.

Baselines. We compare our method with ColorNeRF [10], ColorNeRF-GS, and ChromaDistill [11], where ColorNeRF-GS is our implementation of the method on a 3DGS representation. For ChromaDistill, the configurations in the official code release for 360-degree

Table 1. **Quantitative comparison across datasets** – We provide the quantitative results across all benchmark datasets. The best score is highlighted in **bold**, and the second-best is underlined. Overall, our proposed method achieves the best or second-best result across the majority of scenes. “–” indicates where the NeRF reconstruction failed to converge in 360-degree scenes.

Method	LLFF		Tanks and Temples				Mip-NeRF 360						
	flower	trex	Horse	M60	Train	Truck	bicycle	bonsai	counter	garden	kitchen	room	stump
Color Diversity Index \uparrow													
ColorNeRF	0.1660	0.1250	–	–	0.1680	–	–	<u>0.2090</u>	<u>0.1934</u>	0.1699	0.1777	–	–
ColorNeRF-GS	<u>0.2051</u>	0.0938	<u>0.1543</u>	0.1816	0.2910	<u>0.2539</u>	<u>0.1523</u>	0.1719	0.1699	0.2266	0.1953	0.1660	0.1465
ChromaDistill	0.1211	<u>0.1191</u>	0.1074	<u>0.1387</u>	0.1699	0.1406	0.1230	0.1582	0.1426	<u>0.2363</u>	0.1758	<u>0.1602</u>	0.1074
Ours	0.2754	0.1074	0.1797	0.1309	<u>0.2695</u>	0.3125	0.1582	0.2109	0.2422	0.2793	<u>0.1836</u>	0.1484	<u>0.1309</u>
Short-term consistency \downarrow													
ColorNeRF	0.0002	0.0005	–	–	0.0020	–	–	0.0021	0.0020	0.0016	0.0017	–	–
ColorNeRF-GS	0.0006	<u>0.0002</u>	<u>0.0006</u>	0.0006	0.0017	0.0014	0.0037	0.0012	0.0012	<u>0.0013</u>	0.0015	0.0032	<u>0.0017</u>
ChromaDistill	0.0002	0.0001	0.0002	0.0002	0.0007	0.0002	0.0008	0.0006	0.0006	0.0019	<u>0.0010</u>	0.0038	0.0005
Ours	<u>0.0005</u>	<u>0.0002</u>	<u>0.0006</u>	<u>0.0003</u>	0.0014	<u>0.0008</u>	<u>0.0026</u>	<u>0.0010</u>	<u>0.0010</u>	0.0008	0.0007	0.0017	0.0020
Long-term consistency \downarrow													
ColorNeRF	0.0008	0.0014	–	–	0.0058	–	–	0.0071	0.0073	<u>0.0020</u>	0.0056	–	–
ColorNeRF-GS	0.0037	0.0037	0.0016	0.0024	0.0056	0.0075	0.0036	0.0043	0.0054	<u>0.0020</u>	0.0051	0.0103	<u>0.0019</u>
ChromaDistill	<u>0.0009</u>	0.0003	0.0009	0.0009	0.0030	0.0012	0.0010	0.0020	0.0028	0.0033	<u>0.0035</u>	<u>0.0095</u>	0.0005
Ours	0.0028	<u>0.0005</u>	<u>0.0014</u>	<u>0.0011</u>	<u>0.0052</u>	<u>0.0054</u>	<u>0.0033</u>	<u>0.0034</u>	<u>0.0052</u>	0.0011	0.0030	0.0053	0.0022



Figure 5. **Consistency ablation** – Our global calibration step is essential for mitigating the continuous color shifting artifact observed in uncalibrated views, ensuring global consistency.

scenes do not converge well, resulting in poor optimization. For such scenes, we therefore also use our 3DGS-based implementation.

Evaluation metrics. To evaluate our 3D colorization, we assess both color diversity and color consistency. **1) Color Diversity.** We propose a new metric, the Color Diversity Index (CDI), to quantify the richness of the color distribution in the final 3D scene. To calculate CDI, we first bin the RGB space (0-255) into 8 bins per channel (total $8^3 = 512$ bins). We then populate this 3D histogram with all pixels from the rendered test views of a scene. The CDI is defined as the ratio of bins whose pixel count exceeds a threshold of 100. This metric evaluates how many distinct colors are represented in the 3D scene. **2) Consistency.** To evaluate view consistency, we follow existing works [11, 27] and report both long-term consistency and short-term consistency. **3) Discussed Metrics.** While some works report PSNR against a ground truth [10] or a colourfulness [16] metric, we argue these are not suitable as primary metrics.

Colorization is a one-to-many problem, making PSNR an unreliable indicator of quality. Furthermore, colourfulness metrics often have a preference for overly saturated images. We provide these metrics in the supplementary material for comparison, but focus our main analysis on diversity and consistency.

4.2. Results

Qualitative results. We show example novel views of scenes colorized by our method and the baselines in Fig. 4. As shown, our method colorizes the scenes with plausible and diverse colors. For the forward-facing ‘flower’ scene, our method renders plausible and distinct green tones for the leaves, whereas baseline methods produce a more uniform color, due to an averaging effect. This averaging effect is even more evident in the 360-degree scenes. For instance, in the ‘garden’ scene, baseline methods color all the fruits in the vase green, whereas our method preserves their distinct color. Also note the red cone in the ‘Train’ scene. Furthermore, in indoor scenes, baselines tend to produce a yel-

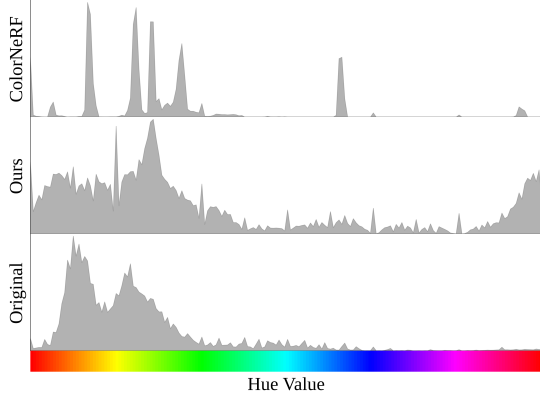


Figure 6. **Hue distribution for the ‘garden’ scene** – Our method preserves diverse and rich colors similar to the original one.

Table 2. **Quantitative ablation on TnT dataset**

Method	CDI \uparrow	short-const. \downarrow	long-const. \downarrow
w/o Flickr8k	0.1689	0.0004	0.0016
$K = 1$	0.2104	0.0024	0.0034
$K = 8$	0.2373	0.0009	0.0034
Ours	<u>0.2231</u>	<u>0.0008</u>	<u>0.0033</u>

lowish cast across the entire scene. In contrast, our method assigns plausible colors to distinct local regions, such as the fruit basket and plant pot in the ‘counter’ scene, and the bicycle in the ‘bonsai’ scene.

Quantitative results. We provide the quantitative results in Tab. 1. Overall, our method demonstrates superior performance across all three metrics. We observe a trade-off in the baseline methods: for instance, while ChromaDistill achieves the highest consistency, its low Color Diversity Index (CDI) reveals this is a consequence of monotonous colorization. In contrast, our method successfully achieves high color diversity while maintaining comparable consistency.

Quantitative analysis. We analyze the distribution of hue in Fig. 6. For the ‘garden’ scene from the Mip-NeRF 360 dataset, we plot a histogram of the hue values from all rendered test view pixels. The y-axis values represent the square-root normalized results. While the distribution for ColorNeRF shows only a few distinct peaks due to color averaging, our result contains a diverse range of hues, similar to the original color scene.

4.3. Ablation studies

The number of subscenes. We conduct an ablation study on the number of subscenes K in Tab. 2 and Fig. 7. As shown, a single base view leads to a degradation in both CDI and consistency compared to $K = 4$. Conversely, in-

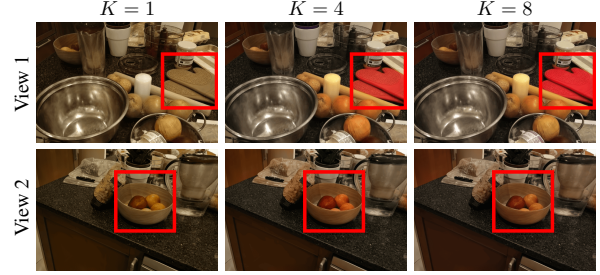


Figure 7. **Ablation on the number of base views** – $K = 1$ fails to colorize the entire scene, due to the lack of color guidance. While $K = 8$ contains rich color, it comes at a cost of the self attention of 8 views. We select $K = 4$ as the optimal value.

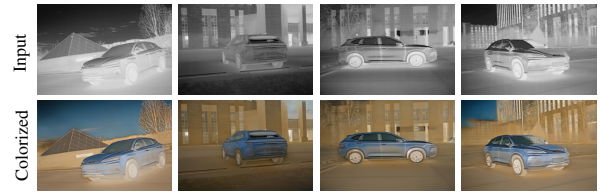


Figure 8. **Result on thermal images** – Our method extends to thermal multi-view images, achieving consistent and realistic colorization beyond grayscale inputs.

creasing to $K = 8$ increases the CDI by providing more color guidance from the image model. However, this also quadruples the computational cost of the reference mixing layer, making $K = 4$ the optimal trade-off between color diversity and computational efficiency.

Global consistency calibration. We demonstrate color consistency across the scene of our method in Fig. 5, by ablating our global calibration process. Without global calibration, the object continuously changes color as the camera moves around the 360-degree scene, leading to unnatural results. In contrast, our method maintains consistent colorization. See suppl. material. for quantitative ablation.

Training data. While the DL3DV-10K-Benchmark is sufficient for learning multi-view referencing, it lacks the broad color distribution required by diffusion models. We thus supplement our training with the Flickr8k dataset to provide this rich color diversity. Our ablation study in Tab. 2 confirms that training on DL3DV alone results in a limited color distribution (see suppl. material for qualitative results).

4.4. Application

To demonstrate that our method is applicable not only to grayscale images but also to general single-channel images, we present results of applying our method to thermal multi-view images. In this case, because the image colorization model cannot colorize thermal images due to the domain

gap in the input images, we replace the image colorization model with ChatGPT5 [40] to translate the base view thermal images into colorized visible images. As shown in Fig. 8, our method successfully achieves plausible and consistent colorization from multi-view single-channel images.

5. Conclusion

In this work, we present *LoGoColor*, a novel approach for colorizing single-channel 3D reconstructions. We identify that existing methods rely on guidance-averaging to achieve multi-view color consistency, which fails to capture the color diversity of complex 360-degree scenes, leading to monotonous results. Our method minimizes this averaging process. However, this leads to a consistency challenge, so we propose a Local-Global pipeline that partitions the scene and uses a fine-tuned multi-view diffusion model to manage both inter-subscene and intra-subscene consistency. Our experiments with our novel Color Diversity Index (CDI) demonstrate that *LoGoColor* produces 3D models that are simultaneously consistent and color-diverse, enhancing their versatility for downstream applications like VR/AR.

References

- [1] Stability AI. SD-Turbo, 2023. 5
- [2] Jonathan T Barron, Ben Mildenhall, Dor Verbin, Pratul P Srinivasan, and Peter Hedman. Mip-nerf 360: Unbounded anti-aliased neural radiance fields. In *Proceedings of the IEEE/CVF conference on computer vision and pattern recognition*, pages 5470–5479, 2022. 2
- [3] Jonathan T Barron, Ben Mildenhall, Dor Verbin, Pratul P Srinivasan, and Peter Hedman. Mip-nerf 360: Unbounded anti-aliased neural radiance fields. In *IEEE Conf. Comput. Vis. Pattern Recog.*, pages 5470–5479, 2022. 6
- [4] M. Cabrelles, S. Galcerá, S. Navarro, J. L. Lerma, T. Akasheh, and N. Haddad. Integration of 3d laser scanning, photogrammetry and thermography to record architectural monuments. In *Proc. 22nd CIPA Symposium*, Kyoto, Japan, 2009. CIPA. 2
- [5] Yuanhao Cai, Yixun Liang, Jiahao Wang, Angtian Wang, Yulun Zhang, Xiaokang Yang, Zongwei Zhou, and Alan Yuille. Radiative gaussian splatting for efficient x-ray novel view synthesis. In *Proceedings of the European Conference on Computer Vision (ECCV)*, pages 111–127, 2024. 2
- [6] Yuanhao Cai, Jiahao Wang, Alan Yuille, Zongwei Zhou, and Angtian Wang. Structure-aware sparse-view x-ray 3d reconstruction. In *Proceedings of the IEEE/CVF Conference on Computer Vision and Pattern Recognition*, pages 13552–13561, 2024. 2
- [7] Xu Cao and Katashi Nagao. Point cloud colorization based on densely annotated 3d shape dataset. In *International Conference on Multimedia Modeling*, pages 436–446. Springer, 2018. 3
- [8] Anpei Chen, Zexiang Xu, Fuqiang Zhao, Xiaoshuai Zhang, Fanbo Xiang, Jingyi Yu, and Hao Su. Mvsnerf: Fast generalizable radiance field reconstruction from multi-view stereo. In *Proceedings of the IEEE/CVF international conference on computer vision*, pages 14124–14133, 2021. 2
- [9] Chia-Yen Chen et al. 3d reconstruction from ir thermal images using silhouette volume intersection. *Infrared Physics & Technology*, 70:104–112, 2015. 3
- [10] Yean Cheng, Renjie Wan, Shuchen Weng, Chengxuan Zhu, Yakun Chang, and Boxin Shi. Colorizing monochromatic radiance fields. In *AAAI*, pages 1317–1325, 2024. 2, 3, 6, 7, 13
- [11] Ankit Dhiman, R Srinath, Srinjay Sarkar, Lokesh R Boregowda, and R Venkatesh Babu. Chromadistill: Colorizing monochrome radiance fields with knowledge distillation. In *IEEE/CVF Winter Conference on Applications of Computer Vision*, pages 2400–2410. IEEE, 2025. 2, 3, 6, 7, 13
- [12] Sara Fridovich-Keil, Alex Yu, Matthew Tancik, Qin-hong Chen, Benjamin Recht, and Angjoo Kanazawa. Plenoxels: Radiance fields without neural networks. In *IEEE Conf. Comput. Vis. Pattern Recog.*, pages 5501–5510, 2022. 1
- [13] Guy Gafni, Justus Thies, Michael Zollhofer, and Matthias Nießner. Dynamic neural radiance fields for monocular 4d facial avatar reconstruction. In *Proceedings of the IEEE/CVF Conference on Computer Vision and Pattern Recognition*, pages 8649–8658, 2021. 1, 2
- [14] Rongrong Gao, Tian-Zhu Xiang, Chenyang Lei, Jaesik Park, and Qifeng Chen. Scene-level point cloud colorization with semantics-and-geometry-aware networks. In *Proceedings-IEEE International Conference on Robotics and Automation*, pages 2818–2824. IEEE, 2023. 3
- [15] Nithin Gopalakrishnan and Vishal M Patel. T2v-ddpm: Thermal to visible face translation using denoising diffusion probabilistic models. In *arXiv preprint arXiv:2209.08814*, 2022. 3
- [16] David Hasler and Sabine Süsstrunk. Measuring colourfulness in natural images. *Proceedings of SPIE—The International Society for Optical Engineering, Human Vision and Electronic Imaging VIII*, 5007:87–95, 2003. 7
- [17] Jonathan Ho, Ajay Jain, and Pieter Abbeel. Denoising diffusion probabilistic models. In *NeurIPS*, pages 6840–6851, 2020. 3

- [18] Micah Hodosh, Peter Young, and Julia Hockenmaier. Framing image description as a ranking task: Data, models and evaluation metrics. *Journal of Artificial Intelligence Research*, 47:853–899, 2013. 6
- [19] Tao Hu, Shu Liu, Yilun Chen, Tiancheng Shen, and Ji-aya Jia. Efficientnerf: Efficient neural radiance fields. In *Proceedings of the IEEE/CVF Conference on Computer Vision and Pattern Recognition*, pages 12902–12911, 2022. 1
- [20] Satoshi Iizuka, Edgar Simo-Serra, and Hiroshi Ishikawa. Let there be color!: Joint end-to-end learning of global and local image priors for automatic image colorization with simultaneous classification. In *SIGGRAPH*, pages 110:1–110:11, 2016. 3
- [21] Dominik Iwaszczuk, Lena Hoegner, and Uwe Stilla. Matching of 3d building models with ir images for texture extraction. In *Proc. Joint Urban Remote Sensing Event (JURSE)*, pages 25–28, Munich, Germany, 2011. IEEE. 2
- [22] Xiaoyang Kang, Tao Yang, Wenqi Ouyang, Peiran Ren, Lingzhi Li, and Xuansong Xie. Ddcolor: Towards photo-realistic image colorization via dual decoders. In *Proceedings of the IEEE/CVF International Conference on Computer Vision (ICCV)*, page 328–338, 2023. 6
- [23] Bernhard Kerbl, Georgios Kopanas, Thomas Leimkühler, and George Drettakis. 3D Gaussian Splatting for Real-Time Radiance Field Rendering. *ACM Trans. Graph.*, 42, 2023. 1, 2, 3
- [24] Arno Knapitsch, Jaesik Park, Qian-Yi Zhou, and Vladlen Koltun. Tanks and temples: Benchmarking large-scale scene reconstruction. *ACM Trans. Graph.*, 36(4):1–13, 2017. 6
- [25] Xiaodong Kuang, Xiubao Sui, Chengwei Liu, Yuan Liu, Qian Chen, and Guohua Gu. Thermal infrared colorization for nighttime driving scenes. In *arXiv preprint arXiv:2104.14374*, 2021. 3
- [26] Disha Kumar, Gaurav Singh, and Yong Man Lee. Colorization transformer. In *ICCV*, pages 16361–16370, 2021. 3
- [27] Wei-Sheng Lai, Jia-Bin Huang, Oliver Wang, Eli Shechtman, Ersin Yumer, and Ming-Hsuan Yang. Learning blind video temporal consistency. In *Eur. Conf. Comput. Vis.*, pages 170–185, 2018. 7
- [28] Xiang Li, Jian Zhang, Xue Bai, and Qing Wang. Near-infrared monocular 3d reconstruction via polarisation imaging. In *Proc. IEEE/CVF Conf. on Computer Vision and Pattern Recognition (CVPR)*, pages 15616–15630. IEEE, 2021. 2, 3
- [29] Zhihao Liang, Qi Zhang, Wenbo Hu, Lei Zhu, Ying Feng, and Kui Jia. Analytic-splatting: Anti-aliased 3d gaussian splatting via analytic integration. In *Euro-pean conference on computer vision*, pages 281–297. Springer, 2024. 2
- [30] Chenguo Lin, Panwang Pan, Bangbang Yang, Zeming Li, and Yadong Mu. Diffsplat: Repurposing image diffusion models for scalable 3d gaussian splat generation. In *International Conference on Learning Representations (ICLR)*, 2025. 2
- [31] Youtian Lin, Zuozhuo Dai, Siyu Zhu, and Yao Yao. Gaussian-flow: 4d reconstruction with dynamic 3d gaussian particle. In *Proceedings of the IEEE/CVF Conference on Computer Vision and Pattern Recognition (CVPR)*, pages 21136–21145, 2024. 1
- [32] Lu Ling, Yichen Sheng, Zhi Tu, Wentian Zhao, Cheng Xin, Kun Wan, Lantao Yu, Qianyu Guo, Zixun Yu, Yawen Lu, Xuanmao Li, Xingpeng Sun, Rohan Ashok, Aniruddha Mukherjee, Hao Kang, Xiangrui Kong, Gang Hua, Tianyi Zhang, Bedrich Benes, and Aniket Bera. D13dv-10k: A large-scale scene dataset for deep learning-based 3d vision. In *Proceedings of the IEEE/CVF Conference on Computer Vision and Pattern Recognition (CVPR)*, page 22160–22169, 2024. 6
- [33] Jitao Liu, Songmin Dai, and Xiaoqiang Li. Pccn: Point cloud colorization network. In *IEEE Int. Conf. Image Process.*, pages 3716–3720. IEEE, 2019. 3
- [34] Y. Liu, X. Zhang, J. Wang, H. Zhao, and F. Xu. Dynamic thermal 3d reconstruction with gaussian splatting. *Remote Sensing*, 17(2):335, 2025. 2, 3
- [35] Ilya Loshchilov and Frank Hutter. Decoupled weight decay regularization. In *International Conference on Learning Representations*, 2019. 5
- [36] Ben Mildenhall, Pratul P. Srinivasan, Rodrigo Ortiz-Cayon, Nima Khademi Kalantari, Ravi Ramamoorthi, Ren Ng, and Abhishek Kar. Local light field fusion: Practical view synthesis with prescriptive sampling guidelines. In *Proceedings of the IEEE/CVF Conference on Computer Vision and Pattern Recognition*, pages 5511–5520, 2019. 6
- [37] Ben Mildenhall, Pratul P Srinivasan, Matthew Tan-cik, Jonathan T Barron, Ravi Ramamoorthi, and Ren Ng. NeRF: Representing Scenes as Neural Radiance Fields for View Synthesis. In *Eur. Conf. Comput. Vis.*, 2020. 1, 2
- [38] Thomas Müller, Alex Evans, Christoph Schied, and Alexander Keller. Instant neural graphics primitives with a multiresolution hash encoding. *ACM transactions on graphics (TOG)*, 41(4):1–15, 2022. 2
- [39] Kamyar Nazeri, Eric Ng, Fahim Joseph, Faisal Qureshi, and Mehran Ebrahimi. Image colorization using generative adversarial networks. In *CVPRW*, pages 708–715, 2018. 3
- [40] OpenAI. Gpt-5 system card. <https://cdn.>

openai.com/gpt-5-system-card.pdf, 2025. Accessed: 2025-11-13. [9](#)

- [41] Gaurav Parmar, Taesung Park, Srinivasa Narasimhan, and Jun-Yan Zhu. One-step image translation with text-to-image models. *arXiv preprint arXiv:2403.12036*, 2024. [3](#), [5](#)
- [42] Ben Poole, Ajay Jain, Jonathan T. Barron, and Ben Mildenhall. Dreamfusion: Text-to-3d using 2d diffusion. *CoRR*, abs/2209.14988, 2022. [1](#)
- [43] Konstantinos Rematas, Ricardo Martin-Brualla, and Vittorio Ferrari. Sharf: Shape-conditioned radiance fields from a single view. *arXiv preprint arXiv:2102.08860*, 2021. [2](#)
- [44] Chitwan Saharia, William Chan, Huiwen Chang, Chris Lee, Jonathan Ho, Tim Salimans, David Fleet, and Mohammad Norouzi. Palette: Image-to-image diffusion models. In *ACM SIGGRAPH 2022 conference proceedings*, pages 1–10, 2022. [3](#), [5](#)
- [45] Axel Sauer, Dominik Lorenz, Andreas Blattmann, and Robin Rombach. Adversarial diffusion distillation. In *Eur. Conf. Comput. Vis.*, pages 87–103. Springer, 2024. [5](#)
- [46] Seunghyeon Seo, Yeonjin Chang, and Nojun Kwak. Flipnerf: Flipped reflection rays for few-shot novel view synthesis. In *Proceedings of the IEEE/CVF International Conference on Computer Vision*, pages 22883–22893, 2023. [2](#)
- [47] Seunghyeon Seo, Donghoon Han, Yeonjin Chang, and Nojun Kwak. Mixnerf: Modeling a ray with mixture density for novel view synthesis from sparse inputs. In *Proceedings of the IEEE/CVF Conference on Computer Vision and Pattern Recognition*, pages 20659–20668, 2023. [2](#)
- [48] Takayuki Shinohara, Haoyi Xiu, and Masashi Matsuoka. Point2color: 3d point cloud colorization using a conditional generative network and differentiable rendering for airborne lidar. In *IEEE Conf. Comput. Vis. Pattern Recog.*, pages 1062–1071, 2021. [3](#)
- [49] Rohit Singh, Shubham Kamat, Oleg Sushkov, Dieter Fox, and Youngwoon Lee. Robot-nerf: A neural radiance field for robotic manipulation. In *Proceedings of the IEEE International Conference on Robotics and Automation (ICRA)*, pages 11223–11230, 2023. [2](#)
- [50] Jiaxiang Tang, Jiawei Ren, Hang Zhou, Ziwei Liu, and Gang Zeng. Dreamgaussian: Generative gaussian splatting for efficient 3d content creation. *arXiv preprint arXiv:2309.16653*, 2023. [2](#)
- [51] Zachary Teed and Jia Deng. Raft: Recurrent all-pairs field transforms for optical flow. In *European conference on computer vision*, pages 402–419. Springer, 2020. [13](#)
- [52] G. A. Wang and et al. Cross-modality paired-images generation for rgb-infrared person re-identification. In *AAAI*, 2020. [3](#)
- [53] Guanjun Wu, Taoran Yi, Jiemin Fang, Lingxi Xie, Xiaopeng Zhang, Wei Wei, Wenyu Liu, Qi Tian, and Xinggang Wang. 4d gaussian splatting for real-time dynamic scene rendering. In *Proceedings of the IEEE/CVF conference on computer vision and pattern recognition*, pages 20310–20320, 2024. [2](#)
- [54] Jing Wu, Jia-Wang Bian, Xinghui Li, Guangrun Wang, Ian Reid, Philip Torr, and Victor Prisacariu. GaussCtrl: Multi-View Consistent Text-Driven 3D Gaussian Splatting Editing. *ECCV*, 2024. [1](#)
- [55] Jay Zhangjie Wu, Yuxuan Zhang, Haithem Turki, Xuanchi Ren, Jun Gao, Mike Zheng Shou, Sanja Fidler, Zan Gojcic, and Huan Ling. Difix3d+: Improving 3d reconstructions with single-step diffusion models. In *IEEE Conf. Comput. Vis. Pattern Recog.*, pages 26024–26035, 2025. [5](#)
- [56] Jinbo Yan, Rui Peng, Luyang Tang, and Ronggang Wang. 4d gaussian splatting with scale-aware residual field and adaptive optimization for real-time rendering of temporally complex dynamic scenes. In *Proceedings of the 32nd ACM International Conference on Multimedia*, pages 7871–7880, 2024. [2](#)
- [57] Zhiwen Yan, Weng Fei Low, Yu Chen, and Gim Hee Lee. Multi-scale 3d gaussian splatting for anti-aliased rendering. In *Proceedings of the IEEE/CVF Conference on Computer Vision and Pattern Recognition*, pages 20923–20931, 2024. [2](#)
- [58] Jiawei Yang, Marco Pavone, and Yue Wang. Freenerf: Improving few-shot neural rendering with free frequency regularization. In *Proceedings of the IEEE/CVF conference on computer vision and pattern recognition*, pages 8254–8263, 2023. [2](#)
- [59] Ziyi Yang, Xinyu Gao, Wen Zhou, Shaohui Jiao, Yuqing Zhang, and Xiaogang Jin. Deformable 3d gaussians for high-fidelity monocular dynamic scene reconstruction. In *Proceedings of the IEEE/CVF conference on computer vision and pattern recognition*, pages 20331–20341, 2024. [2](#)
- [60] Tianxiang Ye, Qi Wu, Junyuan Deng, Guoqing Liu, Liu Liu, Songpengcheng Xia, Liang Pang, Wenxian Yu, and Ling Pei. Thermal-nerf: Neural radiance fields from an infrared camera. In *Proc. IEEE/CVF Conf. on Computer Vision and Pattern Recognition (CVPR)*, pages 1–10. IEEE, 2024. [2](#), [3](#)
- [61] Alex Yu, Ruilong Li, Matthew Tancik, Hao Li, Ren Ng, and Angjoo Kanazawa. Plenotrees for real-time rendering of neural radiance fields. In *Proceedings of the IEEE/CVF international conference on computer vision*, pages 5752–5761, 2021. [2](#)
- [62] Alex Yu, Vickie Ye, Matthew Tancik, and Angjoo Kanazawa. pixelnerf: Neural radiance fields from one

- or few images. In *Proceedings of the IEEE/CVF conference on computer vision and pattern recognition*, pages 4578–4587, 2021. [2](#)
- [63] Zehao Yu, Anpei Chen, Binbin Huang, Torsten Sattler, and Andreas Geiger. Mip-splatting: Alias-free 3d gaussian splatting. In *Proceedings of the IEEE/CVF conference on computer vision and pattern recognition*, pages 19447–19456, 2024. [2](#)
- [64] Yifan Yuan, Xudong He, Xiangyu Ye, Mingming Liu, Jing Zhang, and Dacheng Tao. Nerf-editing: Geometry editing of neural radiance fields. In *Proceedings of the IEEE/CVF Conference on Computer Vision and Pattern Recognition*, pages 18353–18362, 2022. [1](#)
- [65] Ye Yuan, Xueting Li, Yangyi Huang, Shalini De Mello, Koki Nagano, Jan Kautz, and Umar Iqbal. Gavatar: Animatable 3d gaussian avatars with implicit mesh learning. In *Proceedings of the IEEE/CVF conference on computer vision and pattern recognition*, pages 896–905, 2024. [2](#)
- [66] Jingbo Zhang, Xiaoyu Li, Ziyu Wan, Can Wang, and Jing Liao. Text2nerf: Text-driven 3d scene generation with neural radiance fields. *IEEE Transactions on Visualization and Computer Graphics*, 2024. [1](#)
- [67] Richard Zhang, Phillip Isola, and Alexei A. Efros. Colorful image colorization. In *European Conference on Computer Vision (ECCV)*, pages 649–666. Springer, 2016. [3](#), [5](#)
- [68] Yijun Zhang, Kede Ma, and Yinqiang Chen. Bigcolor: Colorization using a big gan. In *ECCV*, pages 345–362, 2022. [3](#)
- [69] Zi-Xin Zou, Zhipeng Yu, Yuan-Chen Guo, Yangguang Li, Ding Liang, Yan-Pei Cao, and Song-Hai Zhang. Triplane meets gaussian splatting: Fast and generalizable single-view 3d reconstruction with transformers. In *Proceedings of the IEEE/CVF conference on computer vision and pattern recognition*, pages 10324–10335, 2024. [2](#)

LoGoColor: Local-Global 3D Colorization for 360° Scenes

Supplementary Material

In this appendix, we provide additional implementation details, a comprehensive analysis, and additional experiments. The supplementary material is organized as follows:

- Sec. A: Limitations
- Sec. B: Implementation details
 - Sec. B.1: Human evaluation details
 - Sec. B.2: Other details
- Sec. C: Experiments
 - Sec. C.1: Consistency and color diversity trade-off
 - Sec. C.2: Human evaluation
 - Sec. C.3: Extended qualitative comparisons
 - Sec. C.4: Extended quantitative comparisons
- Sec. D: Analysis
 - Sec. D.1: Discussion on the metrics
 - Sec. D.2: Extended qualitative ablation
 - Sec. D.3: Extended quantitative ablation
- Sec. E: Video results as HTML

A. Limitations

Our method relies on the capabilities of the image colorization model; consequently, any artifacts or implausible colors generated by the 2D model are inevitably propagated to our 3D result. Furthermore, although we minimize the guidance averaging process, we incorporate a single averaging operation during global calibration. While crucial for establishing global consistency, this step slightly reduces the resulting color diversity.

B. Additional implementation details

B.1. Human evaluation details

We conduct a human evaluation utilizing Amazon Mechanical Turk (AMT) with 100 distinct participants to assess the qualitative plausibility and consistency of our colorization results. For each scene, participants are presented with 4 different views for every tested method and asked to choose the series of images with the most realistic colors. The comparison set consists of four randomized options (ColorNeRF [10], ColorNeRF-GS, ChromaDistill [11], and Ours), with the option count reduced to three where ColorNeRF failed the reconstruction. Crucially, we include an attention check question for data reliability. This involves presenting participants with the true color image alongside three identical, low-saturation options; submissions from participants who fail to select the true color image are filtered out and discarded from the final analysis.

Table S.1. **Human evaluation results** – Our method shows superior overall preference compared to all baselines.

Method	Ours	ColorNeRF	ColorNeRF-GS	ChromaDistill
Preference (%)	48.77	7.00	37.38	6.85

B.2. Other details

We calculate short- and long-term consistency by first rendering the scene using the training view cameras and sorting the resulting frames by sequence order. We set the temporal delta frame to 1 for short-term consistency and 10 for long-term consistency. Following [11], we utilize the RAFT [51] optical flow method; the optical flow is computed on the grayscale version of the rendered images to minimize the impact of color inconsistencies. Consistency metrics are then calculated in the LAB space, using only the AB channels.

Our 3DGS-based ChromaDistill baseline is applied only to scenes where the original ChromaDistill code fails to reconstruct the scene (*i.e.*, the scenes excluding ‘flower’, ‘trex’, and ‘garden’)

For the sake of transparency, we include the implementation code for our 3DGS-based versions of ColorNeRF and ChromaDistill.

C. Experiments

C.1. Consistency and color diversity trade-off

We implement a 3DGS version of ChromaDistill, generally adhering to the settings and methodology described in their official code and paper. However, we encounter a critical trade-off when reproducing their results: reproducing the quantitative scores (Table 2 in [11]) necessitates adjusting the content loss weight¹, which unfortunately results in low color diversity. Conversely, while the specific loss weight in the original code provides higher color diversity, it leads to a significantly degraded consistency. This result is qualitatively shown in Fig. S.1 as ‘CD-modified’, with corresponding quantitative results reported in Tab. S.2 for detailed comparison.

The inability to achieve both color diversity and consistency simultaneously highlights the core challenge of 3D colorization: previous research is forced to achieve consistency by sacrificing color diversity. In contrast, our method overcomes this fundamental trade-off, successfully achieving both consistency and color diversity.

¹This parameter is detailed only in their code. The results presented in our main paper utilize this adjusted content loss weight to ensure fair

Table S.2. **Color Diversity Index and long-term consistency trade-off** – CD-modified exhibits the highest Color Diversity Index (CDI) but simultaneously suffers from the lowest consistency. This result indicates the limitation of the method to maintain consistent color. The artificially high CDI is achieved precisely because the method is inconsistent; the fluctuating colors across different views introduce enough variance to inflate the measured CDI of the scene. This outcome highlights the fundamental trade-off: *existing methods achieve high color diversity only by sacrificing multi-view consistency*.

Method	LLFF		Tanks and Temples				mipnerf360						
	flower	trex	Horse	M60	Train	Truck	bicycle	bonsai	counter	garden	kitchen	room	stump
Color Diversity Index \uparrow													
ChromaDistill	0.1211	0.1191	0.1074	0.1387	0.1699	0.1406	0.1230	0.1582	0.1426	0.2363	0.1758	0.1602	0.1074
CD-modified	0.4355	0.2031	0.2598	0.2910	0.3672	0.3652	0.2422	0.3223	0.2930	0.3594	0.3535	0.2676	0.2500
Ours	0.2754	0.1074	0.1797	0.1309	0.2695	0.3125	0.1582	0.2109	0.2422	0.2793	0.1836	0.1484	0.1309
Long-term consistency \downarrow													
ChromaDistill	0.0009	0.0003	0.0009	0.0009	0.0030	0.0012	0.0010	0.0020	0.0028	0.0033	0.0035	0.0095	0.0005
CD-modified	0.0086	0.0013	0.0024	0.0028	0.0059	0.0053	0.0038	0.0054	0.0074	0.0020	0.0063	0.0152	0.0026
Ours	0.0028	0.0005	0.0014	0.0011	0.0052	0.0054	0.0033	0.0034	0.0052	0.0011	0.0030	0.0053	0.0022



Figure S.1. **Consistency and color trade-off** – ChromaDistill achieves high consistency but lacks color diversity, while CD-modified exhibits sufficient color diversity but suffers from color shifts across views. In contrast, our method successfully overcomes this fundamental limitation, achieving both high color diversity and view consistency.

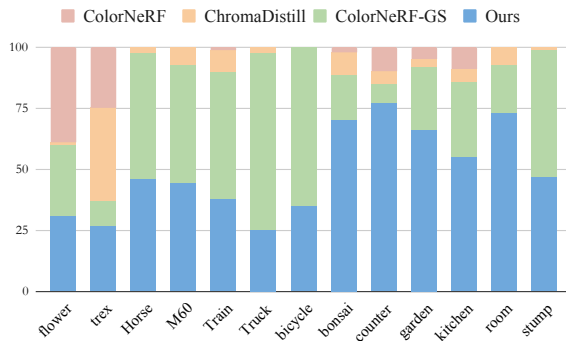


Figure S.2. **Per-scene human evaluation results** – It demonstrates that participant preference for our method is significantly higher in complex 360° scenes than in forward-facing scenes (e.g., ‘flower’, ‘trex’).

quantitative comparison.

C.2. Human evaluation

The human evaluation results in Tab. S.1 indicate that the participants generally perceive our method as having the most realistic and consistent colorization. While a detailed per-scene analysis in Fig. S.2 shows that ColorNeRF-GS achieves competitive scores in certain scenes, these are typically scenes where intricate color details are difficult to evaluate due to the image scale; the true quality discrepancies become visible in the main qualitative comparison (Fig. 4). Furthermore, we observe that on forward-facing scenes such as ‘flower’ and ‘trex’, ColorNeRF also scores comparably. Nevertheless, our method is clearly superior on complex 360° scenes.

C.3. Extended qualitative comparisons

Due to space constraints in the main paper, we provide the complete qualitative results for all scenes in Fig. S.5.



(a) ColorNeRF
Colorfulness = 70.64
Color Diversity Index = 0.1191

(b) Ours
Colorfulness = 61.11
Color Diversity Index = 0.1523

Figure S.3. **Colorfulness** – While the unrealistic, yellowish-cast image (a) registers a high score on the Colorfulness metric, it obtains a low Color Diversity Index. This disparity highlights the superiority of CDI in identifying genuinely diverse color palettes over mere color saturation.

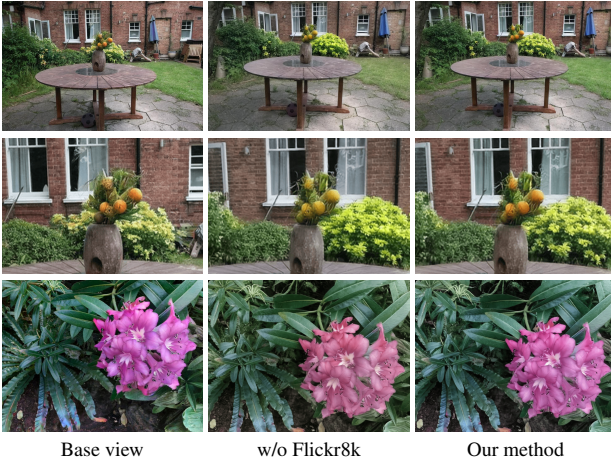


Figure S.4. **Ablation on the training data** – Note the subtle color variations. While the DL3DV-10K-Benchmark dataset is sufficient for training the multi-view referencing capability to the model, it fails to capture the full spectrum of real-world color distribution necessary for plausible colorization. Our method, with the Flickr8k dataset, successfully captures realistic color distribution.

Table S.3. **Quantitative ablation on TnT dataset**

Method	CDI \uparrow	short-const. \downarrow	long-const. \downarrow
w/o calibration	0.2700	0.00081	0.0036
Ours	0.2231	0.00079	0.0033

C.4. Extended quantitative comparisons

As mentioned in the main paper, Tab. S.4 reports additional metrics, including Colorfulness and Peak Signal-to-Noise Ratio (PSNR). While other methods achieve higher Colorfulness scores in some scenes, this is relevant to the inherent limitations of the metric, which we analyze in detail in Sec. D.1.

D. Analysis

D.1. Discussion on the metrics

While the Colorfulness metric generally performs well in evaluating 2D color quality, its utility is compromised in the context of 3D reconstruction due to rendering artifacts. Specifically, when the image model colorizes images containing 3D artifacts, the output often exhibits an unnatural yellowish cast. This distorted, non-plausible color palette paradoxically results in a high Colorfulness score, as shown in Fig. S.3. Comparing (a) and (b) of Fig. S.3 confirms this flaw: the overly yellow image (a) registers a high score, while the image with natural colors (b) registers a low score. This anomaly demonstrates the limitations of the Colorfulness metric for 3D colorization, further validating the need for a dedicated metric, such as our Color Diversity Index.

D.2. Extended qualitative ablation

Training data. While the DL3DV-10K-Benchmark dataset provides crucial multi-view data necessary for referencing capability, its scale of 140 scenes means it cannot adequately represent the full spectrum of real-world color distribution. Since diffusion model performance relies heavily on its learned color space, we supplement our fine-tuning with the Flickr8k dataset to provide this required color diversity. Visually, the impact may be subtle, but the results confirm that incorporating Flickr8k significantly improves its ability to transfer color accurately from the reference base view. This improvement is best observed in zoomed-in views in the second row. The ablation study validating this choice is presented in Fig. S.4.

D.3. Extended quantitative ablation

Tab. S.3 provides the quantitative results for the global consistency ablation shown in Fig. 5, demonstrating that our full method achieves superior consistency.

E. Video results as HTML

For more qualitative results, please see the videos on the supplementary HTML page. The page has no external links and is completely self-contained. These videos clearly show that, unlike other methods where the overall scene color and tone fluctuate with the viewpoint, our approach maintains robust color consistency. We note that these videos are rendered entirely using the 3DGS-based implementation; consequently, the results for some scenes of ChromaDistill differ from the images in the main paper.

Table S.4. **Quantitative comparison across datasets** – Higher is better for \uparrow metrics and lower is better for \downarrow metrics.

Method	LLFF		Tanks and Temples				Mip-NeRF 360						
	flower	trex	Horse	M60	Train	Truck	bicycle	bonsai	counter	garden	kitchen	room	stump
Colorfulness \uparrow													
ColorNeRF	35.92	32.26	–	–	<u>35.05</u>	–	–	49.04	49.18	29.86	53.67	–	–
ColorNeRF-GS	<u>38.33</u>	24.83	<u>23.61</u>	27.26	36.47	46.32	36.01	41.88	44.50	<u>31.56</u>	<u>51.57</u>	52.94	<u>21.10</u>
ChromaDistill	31.00	18.77	8.66	13.14	25.01	14.83	17.35	29.03	31.03	39.30	44.89	<u>49.59</u>	9.63
Ours	40.44	<u>25.81</u>	24.50	<u>19.04</u>	34.28	<u>40.44</u>	<u>31.53</u>	38.87	<u>44.57</u>	27.06	38.87	37.33	25.51
PSNR \uparrow													
ColorNeRF	17.16	<u>22.00</u>	–	–	12.85	–	–	15.43	18.66	17.88	16.16	–	–
ColorNeRF-GS	<u>18.69</u>	22.76	21.78	21.63	19.36	16.70	22.08	19.60	20.91	22.42	18.61	<u>22.60</u>	<u>23.54</u>
ChromaDistill	15.54	21.37	<u>21.42</u>	22.92	<u>19.58</u>	18.75	<u>22.48</u>	21.51	<u>20.87</u>	19.44	<u>18.84</u>	22.58	21.96
Ours	19.19	21.37	21.33	<u>22.34</u>	20.37	<u>16.98</u>	22.92	<u>21.11</u>	20.67	<u>21.78</u>	20.41	24.68	24.78

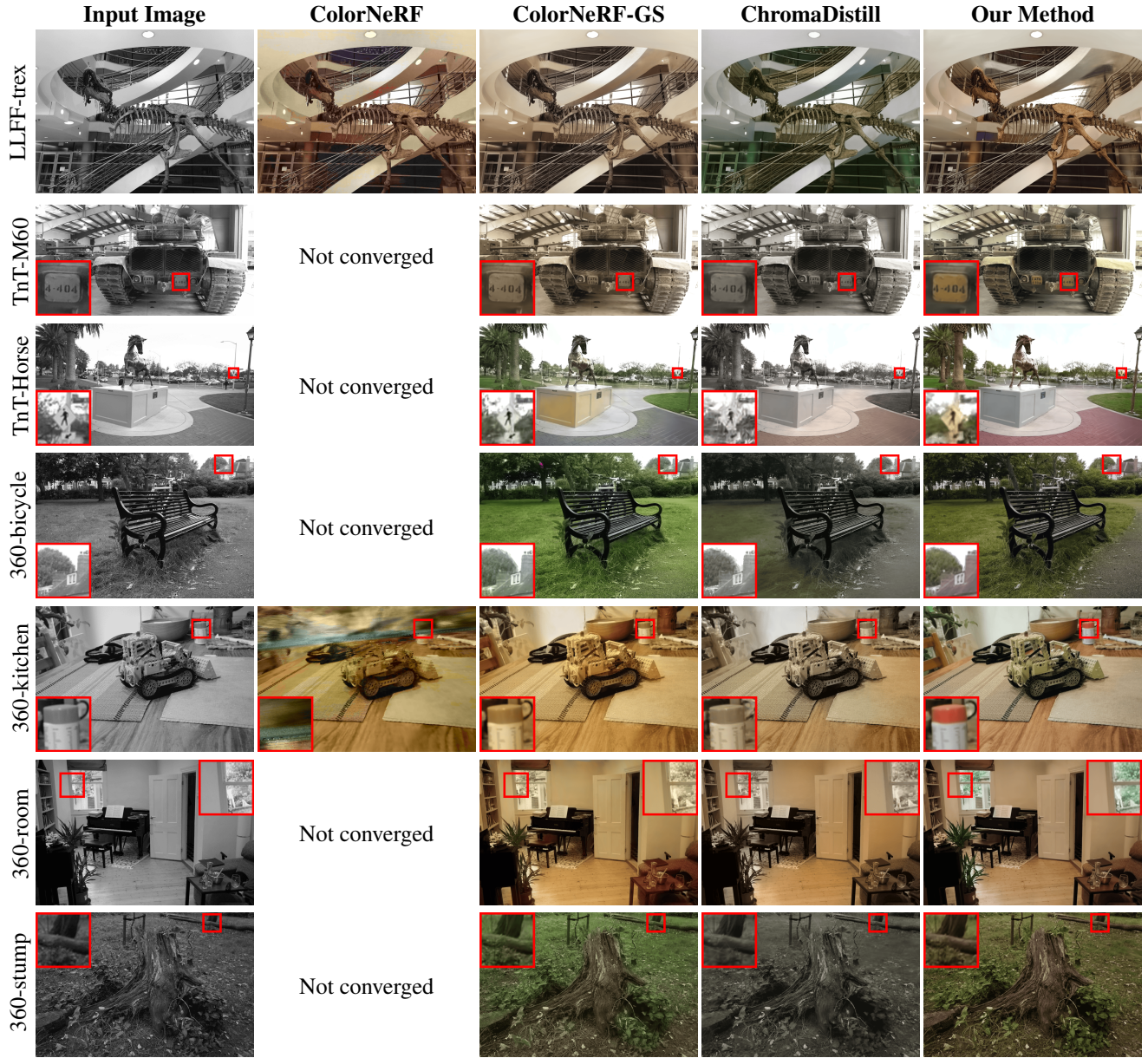


Figure S.5. **Additional qualitative comparison on LLFF, Tanks and Temples (TnT) datasets and Mip-NeRF 360** – We successfully achieve high-fidelity colorization across all parts of the scene, including intricate and fine-grained details.